Electrochimica Acta 525 (2025) 146124

Contents lists available at ScienceDirect

Electrochimica Acta

journal homepage: www.journals.elsevier.com/electrochimica-acta

Thermal decomposition synthesis of Sr-modified ZnS quantum dots for hydrogen peroxide electrochemical sensing

Tanatsaparn Tithito [a], Pranlekha Traiwatcharanon [b], Sarawut Kondee [a], Yotsarayuth Seekaew [b], Gun Chaloeipote [c], Thara Seesaard [d], Pakpoom Reunchan [a], Weeraphat Pon-On [a], Chatchawal Wongchoosuk [a,*]

[a] Department of Physics, Faculty of Science, Kasetsart University, Chatuchak, Bangkok 10900, Thailand
[b] Department of Physics, Faculty of Science, Ramkhamhaeng University, Bang Kapi, Bangkok 10240, Thailand
[c] Division of Physics, Department of Science, Faculty of Science and Technology, Phranakhon Si Ayutthaya Rajabhat University, Phranakhon Si Ayutthaya 13000, Thailand
[d] Department of Physics, Faculty of Science and Technology, Kanchanaburi Rajabhat University, Kanchanaburi 71190, Thailand

ARTICLE INFO

Keywords:
Electrochemical sensors
Quantum dots
H_2O_2 detection
Transition metal chalcogenides
Chemical sensors

ABSTRACT

Hydrogen peroxide (H_2O_2) plays a critical role in various biological, environmental, and industrial processes. However, its excessive accumulation poses significant health and ecological risks. This study presents the synthesis of Sr-modified ZnS quantum dots (Sr@ZnS QDs) via a thermal decomposition method and their application as an innovative sensing material for the electrochemical detection of H_2O_2. The synthesized Sr@ZnS QDs exhibit nanoscale uniformity, high crystallinity, and abundant catalytic active sites, making them ideal candidates for sensor applications. The Sr@ZnS QDs were integrated into screen-printed carbon electrodes, resulting in sensors with exceptional performance. Electrochemical analyses, including cyclic voltammetry, differential pulse voltammetry and chronoamperometry, demonstrated a broad linear detection range (1–80 mM), high sensitivity (12.68 $\mu A \cdot mM^{-1} \cdot cm^{-2}$), and a low detection limit (75.9 μM) at neutral pH. The Sr@ZnS QDs sensor showed excellent selectivity, effectively discriminating H_2O_2 from common interfering species such as NaCl, glucose, and hexane. Furthermore, the proposed catalytic mechanism revealed that the interaction of Sr^{2+} and Zn^{2+} ions with H_2O_2 plays a pivotal role in enhancing the redox reactions. This work introduces Sr@ZnS QDs as a promising material for the development of cost-effective, portable, and high-performance electrochemical sensors. The findings not only advance the field of H_2O_2 sensing but also open new possibilities for the broader application of Sr@ZnS QDs in environmental monitoring, clinical diagnostics, and industrial process control.

1. Introduction

Hydrogen peroxide (H_2O_2) is an inorganic volatile compound and a naturally occurring reactive oxygen species (ROS) in plants [1,2]. It plays a crucial role in various physiological and biochemical processes. Additionally, H_2O_2 is widely used in industrial and clinical applications as a disinfectant [3], bleaching agent [4], water treatment [5], food processing [6] and chemical synthesis [7]. It also serves as a biomarker for evaluating oxidative stress [8,9], cancer biomarkers in early diagnosis [10] and functions as a molecule involved in cellular signaling and the body's defense mechanisms [11,12]. However, excessive accumulation of H_2O_2 can pose serious risks to human health leading to cellular damage [13], atherosclerosis [14], Parkinson's disease [15], Alzheimer's [16], cancer [17] and acute myocardial infarction [18]. Therefore, the accurate, highly sensitive, and rapid detection of H_2O_2 is of great importance and remains a widely studied topic.

Several analytical methods have been reported for the detection and quantification of H_2O_2 such as high-performance liquid chromatography (HPLC) [19], titrimetry [20], colorimetric [21], amperometric [22], chemiluminescence [23], photoelectrochemical [24] and fluorescence [25]. Although these methods provide high accuracy in quantifying H_2O_2, they are often hindered by technical limitations such as the need for expert operation, long analysis times, and the high cost of equipment and reagents. Electrochemical sensors have emerged as an excellent alternative for the selective and sensitive detection of H_2O_2. These sensors provide advantages such as rapid response times, simple

* Corresponding author.
E-mail address: chatchawal.w@ku.ac.th (C. Wongchoosuk).

https://doi.org/10.1016/j.electacta.2025.146124
Received 28 January 2025; Received in revised form 11 March 2025; Accepted 27 March 2025
Available online 28 March 2025

instrumentation, low-cost, portability for field applications, and high sensitivity and selectivity. For examples, Surbhi Sharma et al. [26] fabricated electrochemical sensors for the detection of H_2O_2 in milk and mixed-fruit samples. Irena Mihailova et al. [27] developed an electrochemical sensor based on nanostructured CuO and Co_3O_4 to detect H_2O_2 in Rye sample. Raja Saad Alruwais et al. [28] showed excellent performance of Cu-based MOFs H_2O_2 sensors. Leila Naderi et al. [29] demonstrated non-enzymatic sensor based on a composition of $CuCo_2O_4$ and Co_3S_4 for the electrochemical sensing of H_2O_2 and glucose in human serum. Additionally, electrochemical techniques are highly efficient to acquire more about the dynamic release mechanism of H_2O_2.

Metal nanomaterials such as Zn, Cu, Fe, and their oxides and sulfides have attracted considerable interest as electrochemical sensors and biosensors due to their excellent catalytic properties, remarkable nonenzymatic sensing activities and enhanced stability [30–37]. Zinc sulfide (ZnS) is emerging as a new class of materials for electrochemical sensors due to its wide bandgap, excellent optical and electronic conductivity, non-toxicity, environmental friendliness, and low cost [38, 39]. ZnS can be synthesized in various sizes and structures using inexpensive starting materials making it suitable for diverse catalysis and sensing applications [40]. However, ZnS alone suffers from a high electron and hole recombination rate which limits its efficiency. To overcome this limitation, the incorporation of other materials to form a heterostructure has gained considerable attention. In recent years, composite materials have become a major research focus due to their ability to synergize the beneficial properties of different components leading to enhanced performance for specific applications. In particular, the doping of strontium (Sr) has attracted growing interest because of its ability to enhance catalytic and biological activities [41,42]. Inspired by previous studies, doping of Sr into ZnS is expected to improve charge transport properties, enhance sensitivity and enable faster response times making them ideal candidate of sensing applications.

In this work, we present a thermal decomposition technique to synthesize Sr-modified ZnS quantum dots (Sr@ZnS QDs) which are utilized as an electrochemical platform for the detection of H_2O_2. To the best of our knowledge, this is the first report demonstrating the synthesis and application of Sr@ZnS QDs for H_2O_2 sensing. To enhance the performance of electrochemical sensors, multiple electrodes modified with varying ratios of Sr@ZnS were employed. The developed electrochemical sensors are based on the screen-printed carbon electrodes (SPEs) modified with Sr@ZnS QDs. The sensor's performance was systematically evaluated using cyclic voltammetry (CV), differential pulse voltammetry (DPV) and chronoamperometry (CA) techniques which collectively enabled a comprehensive analysis of its electrochemical behavior. The outstanding performance of the Sr@ZnS QDs sensor can be attributed to its excellent electronic transfer capability. Nyquist impedance measurements confirm that Sr@ZnS QDs exhibit low resistance ensuring rapid electron transfer. Moreover, the sensor has demonstrated ultrasensitive detection of H_2O_2 with a fast response and a low detection limit. This study provides a promising approach for the development of cost-effective, sensitive, and selective electrochemical sensors for H_2O_2 detection at room temperature with the advantage of portability for field applications.

2. Materials and methods

2.1. Chemical reagents

The following chemical reagents were used in this study: zinc acetate ($Zn(CH_3COO)_2{\cdot}2H_2O$, 99.5 %, Q RëC), strontium acetate ($(C_4H_6O_4)Sr$, 99.95 %, Sigma-Aldrich), thioacetamide (98 %, Sigma-Aldrich), 1-octadecene (ODE, technical grade 90 %, Sigma-Aldrich), oleylamine (OLA, technical grade 70 %, Sigma-Aldrich), oleic acid (OA, technical grade 90 %, Sigma-Aldrich), trioctylphosphine (TOP, technical grade 90 %, Sigma-Aldrich) and ethylene glycol (EG). All chemicals were used without further purification.

2.2. Synthesis of the Sr@ZnS QDs

The rapid synthesis of bimetallic sulfides with a narrow particle size distribution remains a challenge for electrochemical sensing, as it is crucial for ensuring a higher number of active sites. In this work, Sr@ZnS QDs were synthesized using a thermal decomposition method without any template precursors as shown in Fig. 1**a**. The chemical formula $Sr_\delta Zn_{1-\delta}S$ was used as the model for synthesis. Four different molar compositions were prepared with the specific amounts of each element detailed in Table S1 of the Supporting Information. Briefly, a mixture of Zn $(CH_3COO)_2{\cdot}2H_2O$ and $(C_4H_6O_4)Sr$ was dissolved in a mixed solution of oleylamine (4.5 mL), 1-octadecene (4.5 mL) and oleic acid (1 mL) in three-necked flask at a temperature of 290 °C under N_2 atmosphere for 30 min. After stirring for 30 min, another solution with a thioacetamide (1 mol) dissolved in 3 mL of TOP was injected into a previously prepared solution. The reaction mixture in the flask was stirred continuously for 15 min. After that, the mixture was cooled down at room temperature. Then, the colloidal Sr@ZnS QDs were centrifuged and washed with ethanol several times. The obtained Sr@ZnS QDs were dried at 60 °C for 1 h. and stored in an incubator for further use.

2.3. Fabrication of the Sr@ZnS QDs electrochemical sensors

The SPEs were modified with Sr@ZnS QDs and configured with carbon as the working electrode (WE), silver/silver chloride (Ag/AgCl) as the reference electrode (RE), and carbon as the counter electrode (CE). The preparation process for the Sr@ZnS QDs-modified SPE is illustrated in Fig. 1**b** 10 mg of Sr@ZnS QDs were dissolved in 1 mL of ethylene glycol. The resulting suspension was ultrasonicated for 15 min to ensure uniform dispersion of the particles. Subsequently, 2.5 μL of Sr@ZnS QDs suspension was dropped on the surface of the SPE WE. The modified SPE electrode was heated at 80 °C for 10 min to evaporate the solvent and enhance the adhesion of Sr@ZnS QDs as a sensing film on the WE [33]. The prepared electrode was then stored at room temperature for further use. The photograph of the finished sensor is displayed in Figure S1 of the Supporting Information.

2.4. Characterizations

The size and shape of the as-prepared Sr@ZnS QDs were examined at the nanoscale using a field-emission transmission electron microscopy (FE-TEM, JEOL/JEM-3100F, Tokyo, Japan). The morphology and chemical composition of the as-prepared Sr@ZnS QDs were characterized using a scanning electron microscope (SEM) and an energy dispersion spectroscopy (EDS) (FEI Quanta 450, Brno, Czech) to observe the morphology and element composition of the samples. The crystal phase composition and crystallinity of the samples were analyzed using X-ray diffractometer (XRD, model: Bruker D8 advance, Karlsruhe, Germany). To determine the surface chemical composition of the Sr@ZnS QDs, X-ray photoelectron spectroscopy (XPS) (AXIS ULTRA^{DLD}, Kratos analytical, Manchester UK) was used.

2.5. Electrochemical measurements

The electrochemical performance of the Sr@ZnS QDs SPEs sensor was determined using cyclic voltammetry (CV), differential pulse voltammetry (DPV), chronoamperometry (CA) and electrochemical impedance spectroscopy (EIS) via a Sensit Smart potentiostat (EmStat Pico module) from PalmSens Bv, Netherlands. The measurements were controlled by a PSTrace Software. All experiments were analyzed by using the electrolytic solution as phosphate-buffered saline (PBS) at pH 7.4 based on screen printed electrode (three electrode system) and connected to a potentiostat under room temperature. The electrical potential (voltage) range was set between 0.9 V and −0.5 V at various scan rates. The volume of solution (H_2O_2, PBS and interferences solution) used for testing was 70 μL.

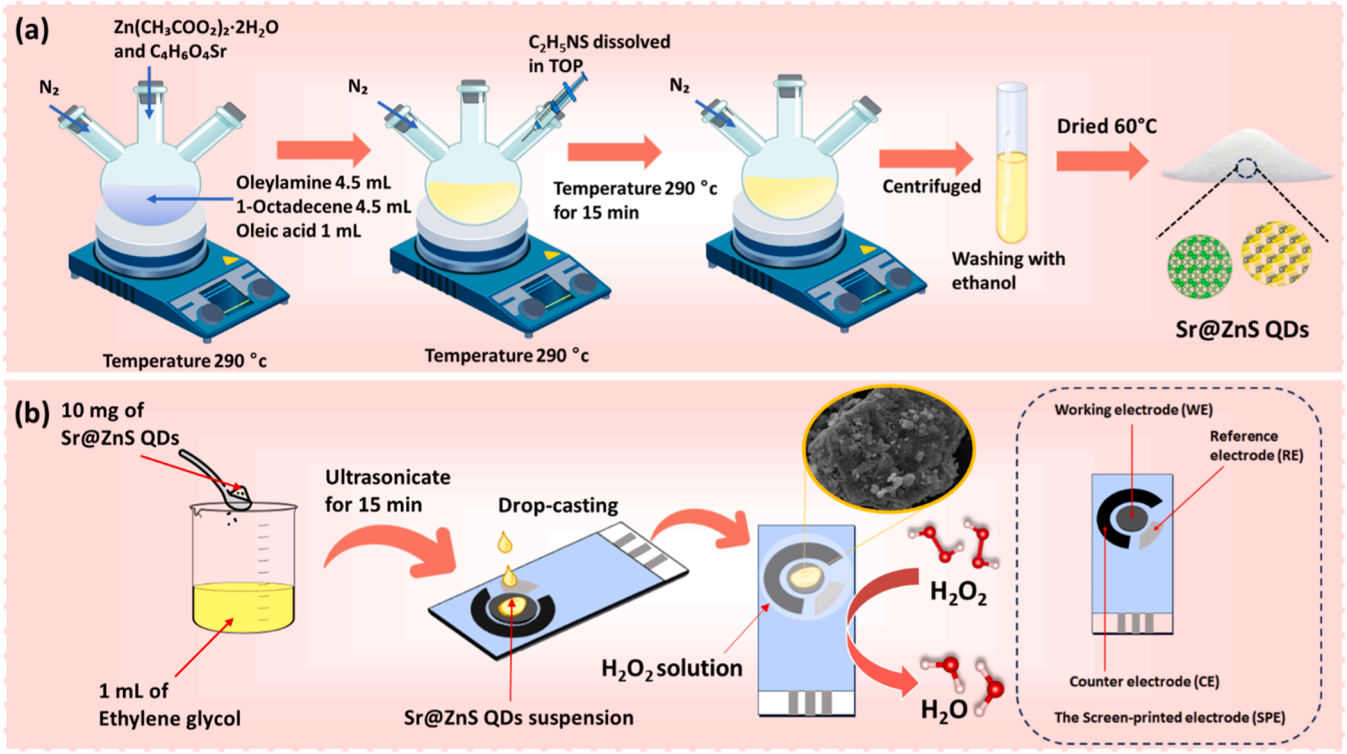

Fig. 1. (a) Schematic illustration of the Sr@ZnS QDs synthesis using thermal decomposition method. (b) Fabrication of the Sr@ZnS QDs modified SPE.

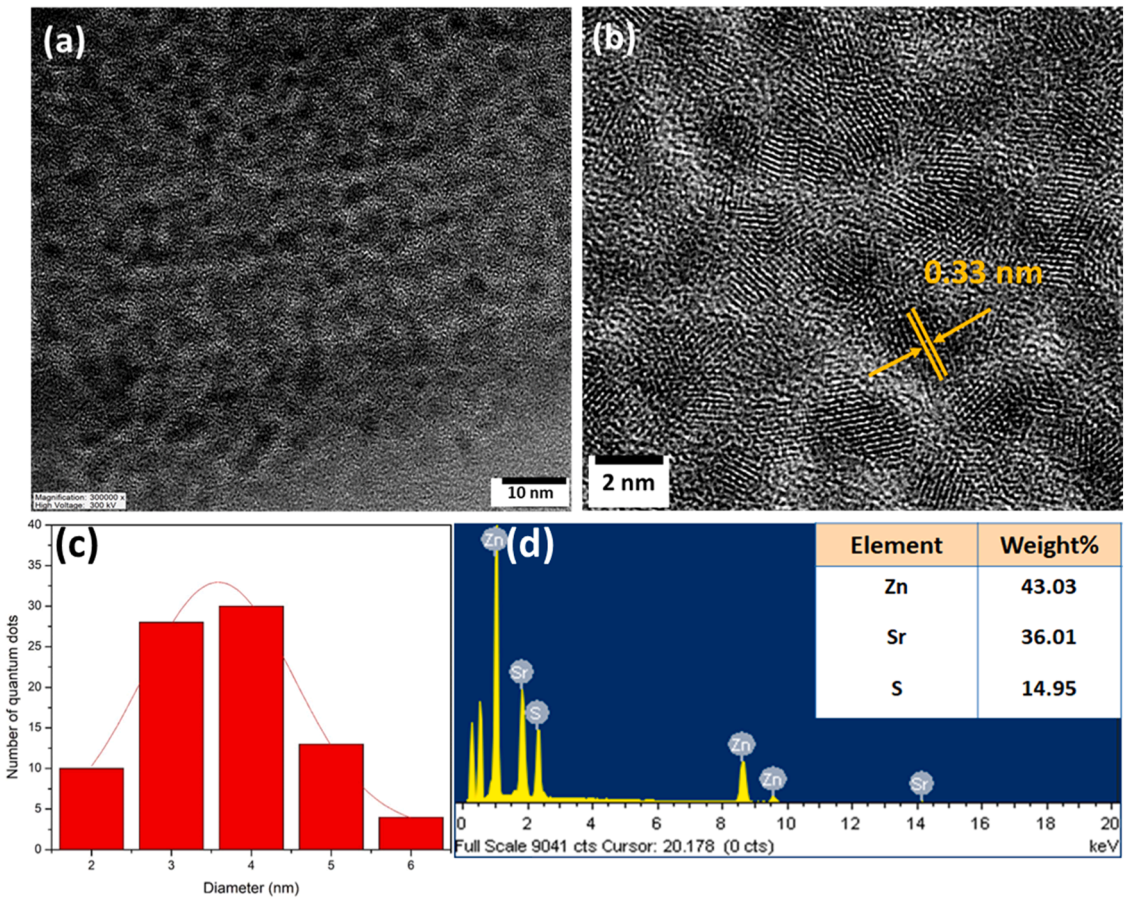

Fig. 2. (a) FE-TEM image, (b) Lattice fringe image, (c) Size distribution, and (d) EDS analysis of synthesized Sr@ZnS QDs.

3. Results and discussion

3.1. Characterization of the Sr@ZnS QDs

The nanoscale size and morphology of Sr@ZnS QDs were characterized using FE-TEM as shown in Fig. 2**a** and Figure S2 of Supporting Information. The Sr@ZnS QDs exhibit a spherical shape with particle diameters ranging from 2 to 6 nm. The average particle size is 3.59 ± 0.95 nm. It demonstrates high uniformity and precise size control achieved through our proposed method. The d-spacing of the lattice was measured as 0.33 nm which corresponds to the (111) diffraction plane of the ZnS as shown in Fig. 2**b** Additionally, EDS analysis (Fig. 2**d**) confirms the presence of main elements including Zn, Sr, and S with weight percentages of 43.03 %, 36.01 %, and 14.95 %, respectively. Elemental mapping (Figure S3 in the Supporting Information) further demonstrates the homogeneous distribution of Zn, Sr, and S within the sample.

The crystalline structures of the synthesized materials were evaluated by XRD analysis. The XRD patterns (Fig. 3) reveal narrow diffraction peaks indicative of a highly crystalline sample. The characteristic diffraction peaks of ZnS are located at 28.7, 47.5 and 56.5° corresponding to the (017), (111) and (207) crystal planes of wurtzite ZnS (JCPDS No 01–089–2136) [43], respectively. The peaks of $SrZn_2$ were identified at 34.4, 36.5, 56.5 and 62.7° corresponding to the (103), (112), (213) and (205) crystal planes of hexagonal $SrZn_2$ (JCPDS No 01–077–4431), respectively. At low Sr doping levels such as Sr@ZnS0.05, no Sr peak is observed suggesting that Sr^{2+} ions are incorporated into the crystallographic sites of Zn^{2+} ions consistent with previous work [44]. However, at higher Sr doping levels, a distinct Sr peak becomes evident. Notably, Sr@ZnS0.25 represents the threshold where a clear Sr peak begins to appear indicating a potential for use as a promising sensing material. This composition may enhance the detection capabilities due to the induced structural modifications within the crystal lattice.

The chemical state and elemental composition of the synthesized Sr@ZnS QDs were examined using XPS as shown in Fig. 4. The wide spectra (Fig. 4**a**) reveal the presence of C 1 s, O 1 s, Zn 2p, Sr 3d and S 2p peaks confirming the incorporation of the expected elements. It should be noted that C 1 s and O 1 s peaks do not correspond to the elements of Sr@ZnS QDs but are commonly observed in XPS analysis. These peaks likely arise from the unavoidable exposure of the material's surface to ambient air and environmental gases containing trace hydrocarbons and oxygen. Such contaminants can adhere to the surface leading to carbon and oxygen signals in the XPS spectra. The high-resolution XPS spectrum of Zn 2p is shown in Fig. 4**b** revealing two distinct spin-orbit components corresponding to Zn $2p_{3/2}$ and Zn $2p_{1/2}$ [45,46]. The Zn $2p_{3/2}$ core level spectra can be divided into two peaks with the binding energies at 1021.1 and 1022.2 eV which are attributed to Zn^{2+} and the hydroxyl group (Zn–OH), respectively [47,48]. Similarly, the Zn $2p_{1/2}$ spectrum exhibits two separate peaks at 1043.7 and 1045.2 eV corresponding to Zn^{2+} valence state [49]. The binding energy difference between the Zn $2p_{3/2}$ and Zn $2p_{1/2}$ are 23.0 eV which aligns closely with the standard reference values for Zn in ZnS. The deconvoluted peaks of S 2p (Fig. 4**c**) were located at the binding energies of 161.7 and 162.9 eV which can be assigned as S $2p_{3/2}$ and $2p_{1/2}$, respectively [50]. These result indicate the presence of S exists as S^{2-} oxidation state within the sample. Fig. 4**d** shows the high-resolution spectrum of Sr 3d with peaks located at binding energies of 133.5 and 135.2 eV which correspond to Sr $3d_{5/2}$ and Sr $3d_{3/2}$, respectively, indicating the presence of the Sr^{2+} state [51]. The XPS analysis can verify the successful synthesis of Sr@ZnS QDs and confirm the incorporation of Sr^{2+}, Zn^{2+}, and S^{2-} ions which are crucial for facilitating interaction with H_2O_2.

The formation of Sr@ZnS QDs through our thermal decomposition synthesis involves the breakdown of a precursor compound at high temperatures. In this work, zinc acetate, thioacetamide, and strontium acetate are used as Zn, S, and Sr precursors, respectively. These precursors are dissolved in a mixture of organic solvents (oleylamine, 1-octadecene, and oleic acid) which serve a dual purpose acting as reaction media and stabilizing agents to prevent particle agglomeration during synthesis. During the heating process at 290 °C, the metal-organic precursor undergoes thermal decomposition. The thermal energy causes the breakdown of the Zn and Sr precursors releasing Zn^{2+} and Sr^{2+} into the solvent. As the temperature rises, the sulfur source decomposes, releasing S atoms into the reaction medium. The sulfur atoms then react with the Zn^{2+} ions to initiate the nucleation of ZnS. The incorporation of Sr^{2+} ions into the ZnS lattice occurs during this stage and is influenced by their ionic radius (1.18 Å) which is larger than that of Zn^{2+} ions (0.74 Å). At low Sr doping levels, Sr^{2+} ions are incorporated into the crystallographic sites of Zn^{2+} within the ZnS lattice. However, at higher doping levels, the Sr^{2+} ions tend to form secondary phases as evidenced by the XRD analysis. This observation suggests that the extent of Sr doping significantly impacts the structural properties of the resulting Sr@ZnS QDs. The growth of Sr@ZnS QDs is governed by a diffusion-controlled process involving Zn^{2+}, Sr^{2+}, and S atoms. Our controlled reaction conditions ensure the formation of high-quality Sr@ZnS QDs with consistent particle size and crystallinity.

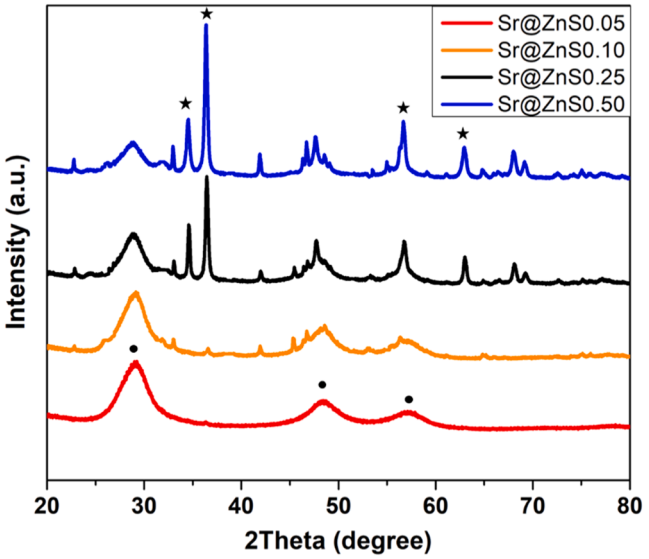

Fig. 3. XRD patterns of the Sr@ZnS QDs with different ratios (• = ZnS phase, ★ = $SrZn_2$ phase).

3.2. Electrochemical characterizations

3.2.1. Electrochemical impedance spectroscopy (EIS)-based studies

To determine the optimal $Sr_\delta Zn_{1-\delta}S$ ratio, the electrochemical activity of both unmodified and Sr@ZnS-modified electrodes at varying ratios was evaluated using electrochemical impedance spectroscopy (EIS) in a solution containing 5 mM $[Fe(CN)_6]^{3-/4-}$ in 0.1 M KCl with a frequency range of 5 Hz to 100 kHz (Fig. 5**a**). It should be noted that KCl was used with $[Fe(CN)_6]^{3-/4-}$ as the electrolyte to enhance conductivity leading to reliable impedance measurements and stable charge transfer [52,53]. For the unmodified sensor, The EIS plot shows a pronounced tail in the low-frequency region with a zoomed view of the high-frequency region in the inset. Notably, the high-frequency tail in the Nyquist plot decreases upon adding Sr@ZnS to the bare SPE indicating a reduction in resistance and suggesting enhanced conductivity of the Sr@ZnS-modified sensors. This suggests that Sr@ZnS contributes to improve electron conduction. The EIS data were fitted to the Randle equivalent circuit for each electrode configuration as illustrated in Figs. 5**b-f**. In the equivalent circuits, R_s, R_{ct}, and R_f represent the series resistance, charge transfer resistance, and interfacial layer resistance, respectively. C_{dl} denotes the double-layer capacitance, W corresponds to the Warburg resistance, and the constant phase element (CPE)

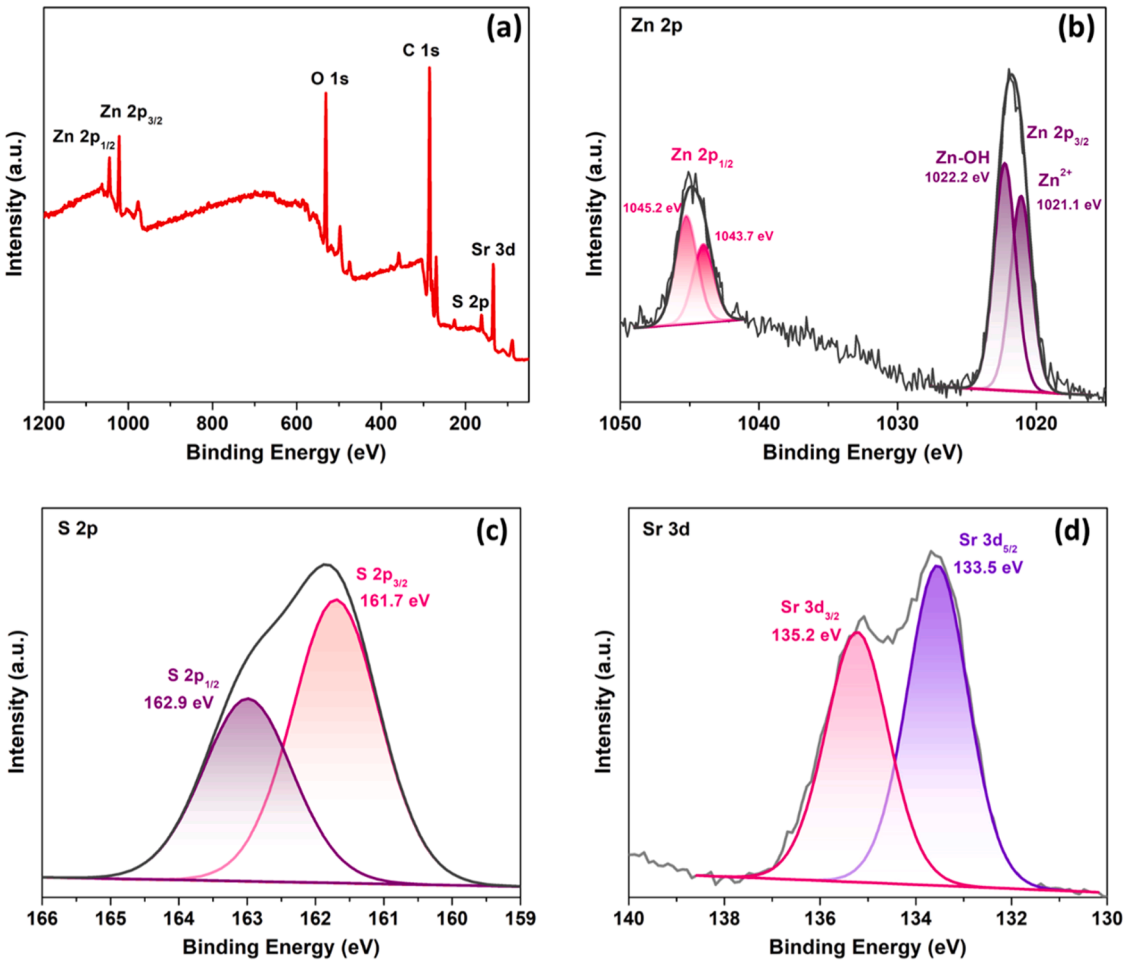

Fig. 4. XPS spectra of the as-prepared Sr@ZnS QDs: (a) wide spectra, (b) Zn 2p, (c) S 2p, (d) Sr 3d.

represents the capacitance associated with a rough surface. The impedance of the CPE described by Eq. (1) is given as:

$$Z\ CPE = 1T(j\omega) \quad (1)$$

where T is related to the capacitance of the CPE. The unit of T is Siemens s^{-1} to the power ϕ. In this study, the constant phase exponent ϕ provides insight into the capacitive behavior of the electrodes. When ϕ=1, the electrode behaves as an ideal capacitor [54]. However, for this experiment, ϕ values were observed as 0.464 for the bare electrode, and 0.868, 0.834, 0.863, and 0.853 for the Sr@ZnS-modified sensors with ratios of 0.05, 0.1, 0.25, and 0.5, respectively. While Sr@ZnS0.25 shows a slightly lower ϕ compared to Sr@ZnS0.05, the Sr@ZnS0.25 exhibits the highest C_{dl} of 3308 nF as shown in Table S2 of the Supporting Information. It suggests that Sr@ZnS0.25 exhibits higher capacitance performance and conductive properties than the other modified electrodes. The R_{ct} values of unmodified and modified electrodes provide a basis for comparing electrode performance. As shown in Table S2 of the Supporting Information, the R_{ct} of the modified electrode decreases significantly from 11,000 Ω for the bare CSPE to 87.87 Ω for the Sr@ZnS0.25-modified electrode. This reduction in R_{ct}, along with an increase in C_{dl}, suggests an expanded electrochemically active surface area for the modified electrode. These enhancements contribute to increased sensitivity for H_2O_2 detection.

3.2.2. *Electrochemical sensing for H_2O_2 detection*

The electrochemical performance at the surface of sensor was investigated using cyclic voltammetry (CV) technique with the applied potential 0.9 to −0.5 V at the scan rate of 0.1 V·s^{-1}. Fig. 6**a** shows comparative investigation of sensors in 10 mM H_2O_2 under PBS solution (pH 7.4). Fig. 6**b,** the CV curves of sensors shows the irreversible oxidation of H_2O_2 process. The bare SPE exhibits the lowest oxidation peak current response. After modifying the surface electrode with the Sr@ZnS, the current intensity increases significantly due to its excellent electrical conductivity properties. The highest oxidation peak current response is observed for the Sr@ZnS0.25 at I_p = 33 μA. Moreover, the potential response at approximately 0.665 V on the Sr@ZnS sensors corresponds to the oxidation of H_2O_2 [55–57]. The enhanced current response of Sr@ZnS0.25 can be attributed to the synergy of bimetallic sulfides and increased dispersion due to zinc strontium sulfide QDs. The FE-TEM image of the Sr@ZnS0.25 nanostructure (as seen in Fig. 2**a**) indicates the accessible sites that promote electron transfer during the electro-oxidation of H_2O_2 [58]. The EDS mapping (Figure S3 of Supporting Information) of the Sr@ZnS nanocomposite demonstrates the uniform dispersion of Sr and Zn elements throughout the nanostructure. This dispersion increases the number of potential active sites and improves electrolytic distribution, thereby enhancing the electrochemical oxidation of H_2O_2. The Zn^{2+}/Sr^{2+}-mediated irreversible electrochemical oxidation reaction in the electrolyte can be summarized as follows:

$$2M^{2+}(M = Sr \text{ or } Zn) + H_2O_2 \leftrightarrow M^{2+} + 2{\cdot}OH + M^{2+} \quad (2)$$

The H_2O_2-sensing mechanism relies on the remarkable electrochemical response of the sensor which arises from the interaction between H_2O_2 molecules and the Sr@ZnS nanostructures on the electrode surface. The synthesized Sr@ZnS acts as an efficient nanozyme offering abundant catalytic active sites that serve dual purposes: providing sample surface sites for H_2O_2 adsorption and facilitating numerous

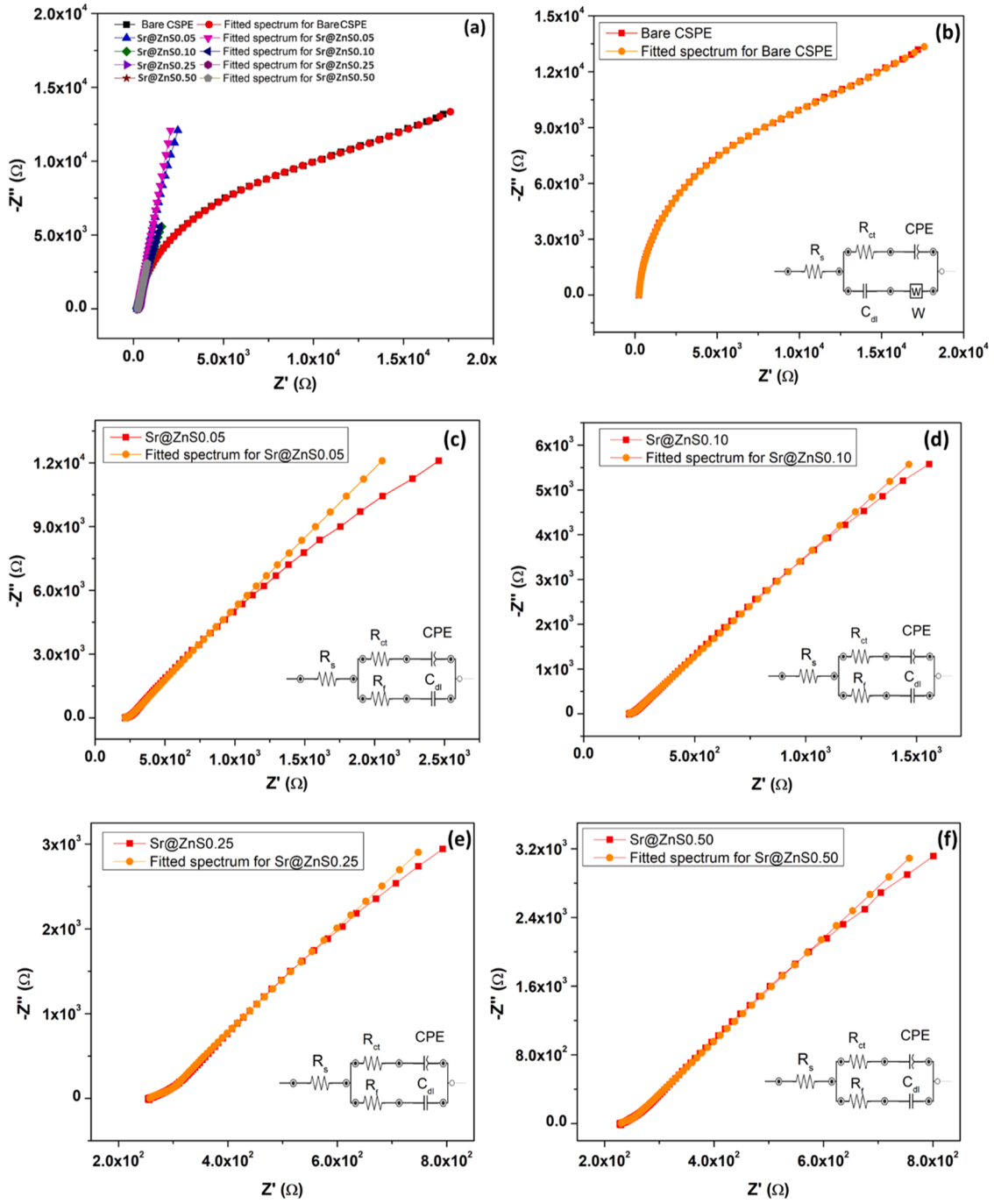

Fig. 5. (a) Nyquist plots of bare SPE, Sr@ZnS0.05, Sr@ZnS0.10, Sr@ZnS0.25 and Sr@ZnS0.50-based sensors in a solution of 5 mM of $[Fe(CN)_6]^{3-/4-}$ in 0.1 M KCl. The EIS plots and the fitted spectra with a corresponding equivalent circuit of (b) the bare CSPE, (c) the Sr@ZnS0.05 (d) the Sr@ZnS0.10, (e) the Sr@ZnS0.25 and (f) the Sr@ZnS0.50 modified on SPE.

electroactive sites for the redox reactions of H_2O_2. These synergistic properties significantly enhance the sensor's performance. The electrocatalytic reduction of H_2O_2 is governed by two critical processes: adsorption and electron transfer. The proposed catalytic mechanism of Sr@ZnS nanozymes is illustrated in Fig. 7. In essence, in solution, the HO–OH bond of H_2O_2 is cleaved on the surface of the nanozymes by surface-bound Sr^{2+} and Zn^{2+} ions, generating adsorbed hydroxyl radicals (•OH ads) as described in Eq. (3)- Eq (7). This mechanism underscores the efficiency of Sr@ZnS nanozymes in accelerating the redox reaction of H_2O_2 offering a promising approach for advanced sensor applications.

Absorption process:

$$Sr@ZnS + H_2O_2 \leftrightarrow Sr@ZnS{\cdot}H_2O_2 \quad (3)$$

or

$$2M^{2+}(M = Sr \text{ or } Zn) + H_2O_2 \leftrightarrow M^{2+}\text{--}OHHO\text{--}M^{2+} \quad (4)$$

Dissociation process:

$$M^{2+}\text{--}OHHO\text{--}M^{2+} \leftrightarrow M^{3+}\text{---}OHHO\text{---}M^{3+} \quad (5)$$

$$M^{3+}\text{---}OHHO\text{---}M^{3+} \leftrightarrow 2M^{3+} + 2OH^- \quad (6)$$

$$\text{Overall reaction}: H_2O_2 + 2e^- \leftrightarrow 2OH^- \quad (7)$$

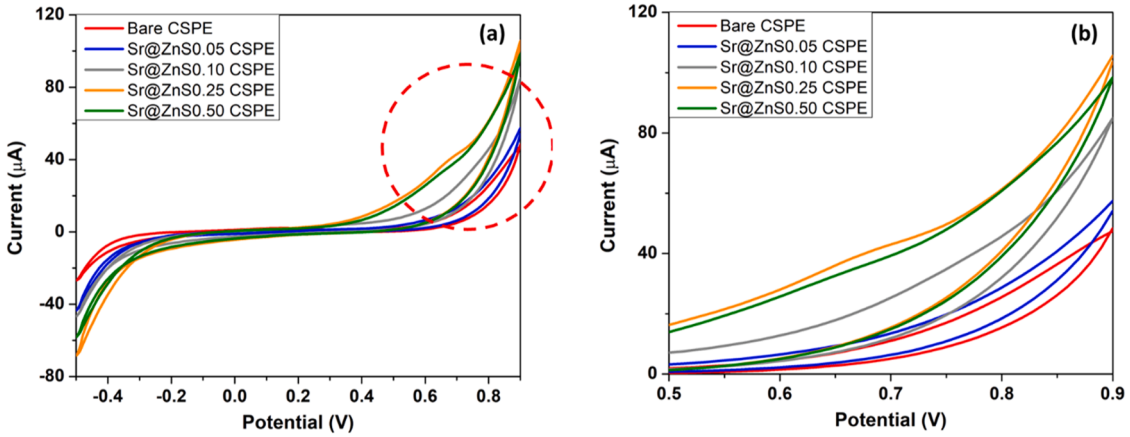

Fig. 6. Cyclic voltammetry curves of (a) the unmodified, Sr@ZnS0.05, Sr@ZnS0.10, Sr@ZnS0.25 and Sr@ZnS0.50 sensors for 10 mM H_2O_2 at potential 0.9 to −0.5 V and (b) zoom in range from 0.5 to 0.9 V.

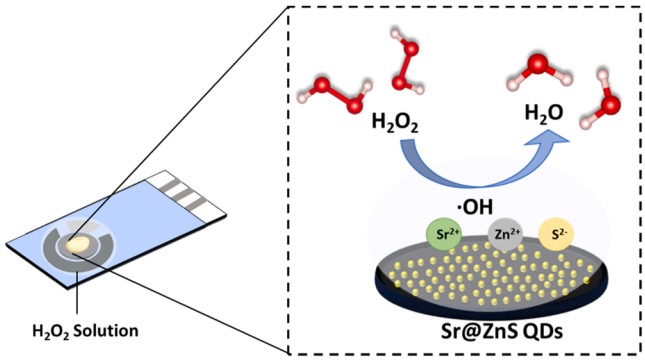

Fig. 7. H_2O_2 sensing mechanism of the Sr@ZnS modified electrode.

3.2.3. *Effect of scan rate*

The optimum Sr@ZnS0.25 sensors were further used at different scan rate ranging from 0.05 to 0.10 $V{\cdot}s^{-1}$ with 10 mM H_2O_2 in PBS solution (pH 7.4) as shown in Figure S4(a) of the Supporting Information. It was found that a changing of the scan rate causes two key phenomena:

(i) The current response ($I(\mu A)$) increases linearly with the scan rate as shown in Figure S4(b) of the Supporting Information. The corresponding linear regression equation for the oxidation process can be expressed in Eq. (8).

$$\text{Oxidation}: \ I = 121.18\ V^{1/2} - \ 7.2505 \ \left(R^2 = 0.933\right) \tag{8}$$

(ii) A shifting of potentials is also observed. These observations suggest that the reaction is a diffusion-controlled process [59].

In order to consider the electron-transfer kinetics of H_2O_2 oxidation behaviour at the surface of the Sr@ZnS0.25 sensors, the effect of scan rates was studied using the standard supporting electrolyte solution of $[Fe(CN)_6]^{3-/4-}$. Figure S4(c) in Supporting Information represent the influence of scan rates in ranging from 0.03 to 0.10 $V{\cdot}s^{-1}$ to 10 mM H_2O_2 in 5 mM $[Fe(CN)_6]^{3-/4-}$. From the CV curves, it can be observed that a well-defined redox peaks are present and the current intensity increases with increasing scan rate according to the previous results [60,61]. The linear plot of redox current response ($I(\mu A)$) and square root of scan rate ($V^{1/2}$) is shown in Figure S4(d) of the Supporting Information. The linear regression equations for the oxidation and reduction processes demonstrate a strong correlation with correlation coefficient of 0.995 and 0.991, respectively. The linear regression equation for oxidation and reduction process are obtained as follow Eq. (9) and Eq. (10).

$$\text{Oxidation reaction}: \ I = 74.7906\ V^{1/2} + 8.89567 \tag{9}$$

$$\text{Reduction reaction}: \ I = -93.7576\ V^{1/2} - 5.73211 \tag{10}$$

Furthermore, the slope at oxidation process from linear regression equation can be used to calculate the electrochemical active surface area of 0.020 cm^2 using the Randles–Sevcik formula as shown in Eq. (11).

$$I_P = \ \left(2.69\ \times 10^5\right) n^{\frac{3}{2}} A D^{\frac{1}{2}} C v^{\frac{1}{2}} \tag{11}$$

Where $I_P\ (A)$ represents the highest oxidation peak current, n represents the number of electrons transferred in the redox reaction, $A\ (cm^2)$ represents the electrochemically active surface area, F $\left(C{\cdot}mol^{-1}\right)$ represents the Faraday constant as 96485.3321, $D\ \left(cm^2{\cdot}s^{-1}\right)$ represents the diffusion coefficient of $[Fe(CN)_6]^{3-/4-}$as 7.6 $\times\ 10^{-6}$, $C\ \left(mol{\cdot}cm^{-3}\right)$ represents the concentration of $[Fe(CN)_6]^{3-/4-}$, $V\ \left(V{\cdot}s^{-1}\right)$ represents the scan rate, $R\ \left(J{\cdot}K^{-1}{\cdot}mol^{-1}\right)$ represents the gas constant as 8.314462 and T (K) is the temperature as 298.15 K.

3.2.4. *Sensitivity*

Differential pulse voltammetry (DPV) is one of the precision techniques for determining sensor performance due to its advantage of low capacitive current, which enhances the sensitivity of the voltammetric procedure. Therefore, DPV is used to analyze the sensitivity of the sensor. The sensing performance of Sr@ZnS0.25 sensors was tested at various concentrations of H_2O_2 from 1–80 mM in PBS buffer (pH 7.4) by using DPV technique at scan rate 0.05 $V{\cdot}s^{-1}$ as shown in Fig. 8**a**. It was clearly observed that the current intensity response increases proportionally with the concentration of H_2O_2. Fig. 8**b** shows the calibration curve between concentration (C_{H2O2}(mM)) and current response ($I(\mu A)$) with a high correlation coefficient of 0.9929. The linear regression equation from DPV curve is expressed in Eq. (12).

$$I = 0.88218\ C_{H_2O_2} + 33.8423 \tag{12}$$

From the linear regression equation, the sensitivity of the sensor (S) is calculated to be 12.68 $\mu A{\cdot}mM^{-1}{\cdot}cm^{-2}$ which is according to Eq. (13).

$$S = \ m/A \tag{13}$$

where $m\ \left(\mu A{\cdot}mM^{-1}\right)$ represents the slope of the linear regression equation and $A\ \left(cm^2\right)$ represents a geometric surface area of the bare SPE as 0.07065 cm^2.

The limit of detection (LOD) can calculated to be 75.9 μM as following in Eq. (14).

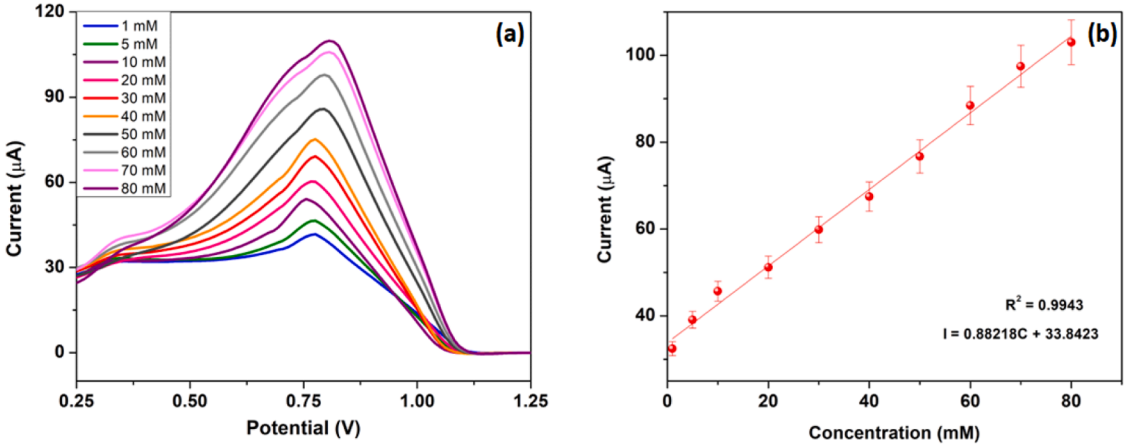

Fig. 8. (a) Differential pulse voltammetry responses of the Sr@ZnS QDs sensors at various H_2O_2 concentrations (PBS buffer pH 7, scan rate 50 $mV{\cdot}s^{-1}$). (b) Calibration plot between cathodic peak currents and H_2O_2 concentrations.

$$LOD = 3SD/m \tag{14}$$

where *SD* represents the standard deviation of blank and *m* represents the slope of the linear regression equation. The obtained results were compared with those of other sensing nanomaterials demonstrating superior performance as summarized in Table 1.

3.3. Selectivity

Chronoamperometry (CA) technique was selected for the measurement. This technique applies a constant pulse potential to the working electrode enabling confirmation of the sensor's selectivity toward H_2O_2. As shown in Fig. 9**a**, the Sr@ZnS0.25 sensor selectivity was tested using H_2O_2 and potential interfering solutions including NaCl, glucose, hexane and $Mg(NO_3)_2$ at a constant potential of 0.77 V. All sample solutions were prepared at a concentration of 10 mM and each interfering substance was added every 60 s. The CA demonstrates that H_2O_2 exhibits a significantly higher response than other interfering solutions. Fig. 9**b** present the histogram of recovery (%) NaCl, glucose, hexane and Mg $(NO_3)_2$ in the range of 85.7 %−95.6 %. Therefore, it confirm the high selectivity and productivity of Sr@ZnS0.25 sensors toward H_2O_2. For the recovery (%) can be calculated using Eq. (15).

$$\%\ Recovery = \left(\frac{I_s - I_U}{I_s}\right) \times 100\% \tag{15}$$

Where I_s (μA) is current response for H_2O_2 solution detection, I_U (μA) is current response for interfering solution detection.

Table 1
Comparison of the analytical performance of electrochemical H_2O_2 sensors.

Sensing material	Linear range (mM)	Sensitivity ($\mu A{\cdot}mM^{-1}{\cdot}cm^{-2}$)	LOD (μM)	Ref
α-Fe_2O_3 microsnowflake	0.1–5.5	7.16	10	[62]
Ag-Au/Cu_2O	0–1.4	4.16	1.3	[63]
Ag/UTPNSs	0.0193–90	4.477	0.57	[64]
Si_3N_4-FET	10–100	–	10,000	[65]
FET	0.1–10	–	100	[66]
Pt/OMC/Au	–	6.83	42	[67]
$NiFe_2$/OMC	0.06–42.7	4.29	0.24	[68]
Fe_2O_3/GC	10–150	2.5	7	[69]
Au-PANI nanowires	5–40	–	5000	[70]
MWCNTPANI nanowires	1–20	–	1000	[71]
Ag-Cu nanoalloys	0.152–0.19	–	152	[72]
Metal doped CNT	0.3–0.75	–	430	[73]
Sr@ZnS QDs	1–80	12.68	75.9	This work

Notes;.
Ag/UTPNSs = ultra-thin polypyrrole nanosheets with Ag nanoparticles.
FET = field-effect transistor.
OMC = ordered mesoporous carbon.
PANI = polyaniline.
MWCNTPANI nanowires = multi-walled carbon nanotube polyaniline nanowires.

4. Conclusion

In summary, Sr@ZnS QDs were successfully synthesized using a thermal decomposition method and applied as an electrochemical sensing material for H_2O_2 detection. The synthesized Sr@ZnS QDs demonstrates remarkable structural and electrochemical properties including uniform particle size, high crystallinity, and a rich density of catalytically active sites which contribute to their superior sensing capabilities. Our proposed thermal decomposition method also provides a scalable, reproducible, and cost-effective route for producing Sr@ZnS QDs which can facilitate large-scale manufacturing for industrial sensor applications. The Sr@ZnS QDs-modified screen-printed electrode exhibits a high sensitivity of 12.68 $\mu A{\cdot}mM^{-1}{\cdot}cm^{-2}$ with a low LOD of 75.9 μM. The EIS and CA analyses reveal superior electron transfer kinetics and exceptional selectivity toward H_2O_2, even in the presence of common interfering substances such as NaCl, glucose, and hexane. The proposed electrocatalytic mechanism demonstrates that the synergy between Sr^{2+} and Zn^{2+} ions played a vital role in cleaving the HO–OH bond of H_2O_2 and facilitating the redox process. These findings establish Sr@ZnS QDs as a promising material for developing cost-effective, portable, and high-performance electrochemical sensors suitable for real-time H_2O_2 monitoring in environmental, industrial, and biomedical applications. Future research can explore further optimization of Sr@ZnS QDs by integrating them with flexible and wearable sensor platforms, enhancing their applicability in smart sensing technologies.

CRediT authorship contribution statement

Tanatsaparn Tithito: Writing – original draft, Visualization, Methodology, Formal analysis, Data curation. **Pranlekha Traiwatcharanon:** Writing – original draft, Methodology, Investigation, Formal analysis. **Sarawut Kondee:** Methodology, Investigation. **Yotsarayuth Seekaew:** Formal analysis. **Gun Chaloeipote:** Formal analysis. **Thara Seesaard:** Formal analysis. **Pakpoom Reunchan:** Visualization. **Weeraphat Pon-On:** Formal analysis. **Chatchawal Wongchoosuk:** Writing – review & editing, Validation, Supervision, Software, Resources, Methodology, Investigation, Funding acquisition, Formal analysis, Conceptualization.

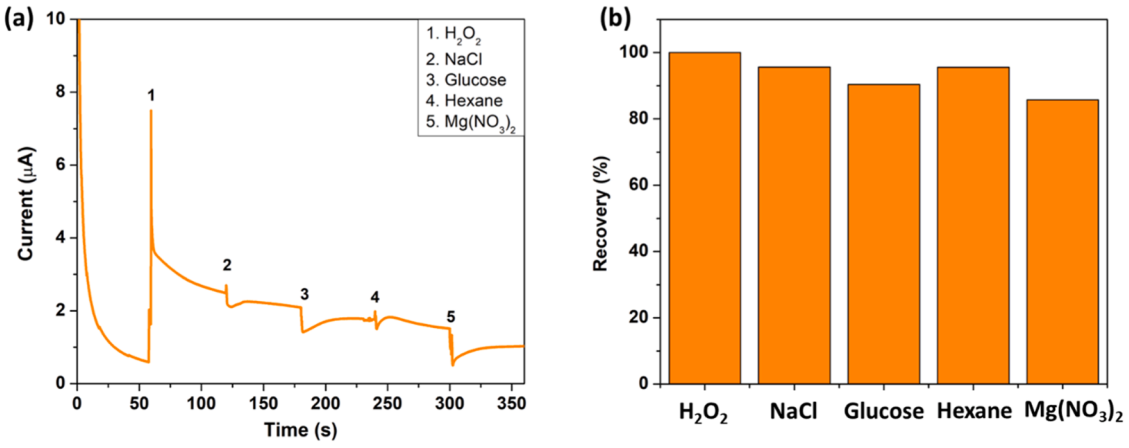

Fig. 9. (a) Dynamic chronoamperometric current responses of the Sr@ZnS sensor to various interfering species. (b) Average % recovery of the Sr@ZnS sensors (five sensors).

Declaration of competing interest

The authors declare that they have no known competing financial interests or personal relationships that could have appeared to influence the work reported in this paper.

Acknowledgments

This research has received funding support from the NSRF via the Program Management Unit for Human Resources & Institutional Development, Research and Innovation (grant number B13F670065) and Kasetsart University Research and Development Institute (FF(KU) 51.67).

Supplementary materials

Supplementary material associated with this article can be found, in the online version, at doi:10.1016/j.electacta.2025.146124.

Data availability

Data will be made available on request.

References

[1] C. Lei, M. Ye, C. Li, M. Gong, H_2O_2 participates in the induction and formation of potato tubers by activating tuberization-related signal transduction pathways, AG 13 (2023) 1398, https://doi.org/10.3390/agronomy13051398.
[2] S. Jaiswal, D.K. Tripathi, R. Gupta, F.J. Corpas, V.P. Singh, HPCA1: a H_2O_2 sensor mediating biotic and abiotic stress resilience in plants, Plant Growth Regul. 43 (2024) 365–368, https://doi.org/10.1007/s00344-023-11055-3.
[3] C. Tao, X. Tang, Y. Gan, Y. Qin, S. Yang, F. Huang, Investigation of the disinfection efficiency of commercial hydrogen peroxide, chlorine dioxide, and chlorine disinfectant on different surfaces, AJVR 85 (2024), https://doi.org/10.2460/ajvr.24.03.0079.
[4] A. Walawska, M. Olak-Kucharczyk, A. Kaczmarek, M.H. Kudzin, Environmentally friendly bleaching process of the cellulose fibres materials using ozone and hydrogen peroxide in the gas phase, Mater. 17 (2024) 1355, https://doi.org/10.3390/ma17061355.
[5] I. Sánchez-Montes, G.O.S. Santos, T.O. Silva, R. Colombo, M.R.V. Lanza, An innovative approach to the application of electrochemical processes based on the in-situ generation of H_2O_2 for water treatment, J. Clean. Prod. 392 (2024) 136242, https://doi.org/10.1016/j.jclepro.2023.136242.
[6] J. Dong, X. Ouyang, B. Huo, D. Deng, X. Yan, L. Luo, CuO/CoZn-layered double-hydroxide nanowires on carbon cloth as an enzyme-free H_2O_2 sensor, ACS. Appl. Nano Mater. 7 (2024) 6564–6573, https://doi.org/10.1021/acsanm.4c00388.
[7] L. Han, L. Tang, D. Deng, H. He, M. Zhou, L. Luo, A novel hydrogen peroxide sensor based on electrodeposited copper/cuprous oxide nanocomposites, Anal 2 (2019) 685–690, https://doi.org/10.1039/C8AN01876F.
[8] H. Xie, Y. Cheng, Y. Cai, T. Ren, B. Zhang, N. Chen, J. Wang, A H_2O_2-specific fluorescent probe for evaluating oxidative stress in pesticides-treated cells, rice roots and zebrafish, J. Hazard. Mater. 465 (2024) 133426, https://doi.org/10.1016/j.jhazmat.2024.133426.
[9] K. Jomova, R. Raptova, S.Y. Alomar, S.H. Alwasel, E. Nepovimova, K. Kuca, M. Valko, Reactive oxygen species, toxicity, oxidative stress, and antioxidants: chronic diseases and aging, Arch. Toxicol. 97 (2023) 2499–2574, https://doi.org/10.1007/s00204-023-03562-9.
[10] L. Long, H. Liu, X. Liu, L. Chen, S. Wang, C. Liu, S. Dong, J. Jia, Co-embedded N-doped hierarchical carbon arrays with boosting electrocatalytic activity for in situ electrochemical detection of H_2O_2, Sens. Actuators. B Chem. 318 (2020) 128242, https://doi.org/10.1016/j.snb.2020.128242.
[11] I.Z. Sadiq, Free radicals and oxidative stress: signaling mechanisms, redox basis for Human diseases, and cell cycle regulation, Curr. Mol. Med. 23 (2023) 13–35, https://doi.org/10.2174/1566524022666211222161637.
[12] A.B. Jena, R.R. Samal, N.K. Bhol, A.K. Duttaroy, Cellular Red-ox system in health and disease: the latest update, Biomed. PharmacOther 162 (2023) 114606, https://doi.org/10.1016/j.biopha.2023.114606.
[13] M. Shao, Y. Wang, H. Dong, L. Wang, X. Zhang, X. Han, X. Sang, Y. Bao, M. Peng, Cao G, From liver fibrosis to hepatocarcinogenesis: role of excessive liver H2O2 and targeting nanotherapeutics, Bioact. Mater. 23 (2023) 187–205, https://doi.org/10.1016/j.bioactmat.2022.11.001.
[14] X. Liang, H. Li, X. Li, X. Tian, A. Zhang, Q. Luo, J. Duan, Y. Chen, L. Pang, C. Li, X. J. Liang, Y. Zeng, J. Yang, Highly sensitive H2O2-scavenging nano-bionic system for precise treatment of atherosclerosis, Acta Pharm. Sin. B 13 (2023) 372–389, https://doi.org/10.1016/j.apsb.2022.04.002.
[15] S. Hassani, A. Esmaeili, The neuroprotective effects of ferulic acid in toxin-induced models of Parkinson's disease: a review, Ageing Res. Rev. 97 (2024) 102299, https://doi.org/10.1016/j.arr.2024.102299.
[16] M. Perluigi, F.D. Domenico, D.A. Butterfield, Oxidative damage in neurodegeneration: roles in the pathogenesis and progression of Alzheimer disease, Physiol. Rev. 104 (2024) 103–197, https://doi.org/10.1152/physrev.00030.2022.
[17] T. Ahmad, A. Iqbal, S.A. Halim, J. Uddin, A. Khan, S.E. Deeb, A. Al-Harrasi, Recent advances in electrochemical sensing of hydrogen peroxide (H_2O_2) released from cancer cells, J. Nanomater. 12 (2022) 1475, https://doi.org/10.3390/nano12091475.
[18] J. He, D. Liu, L. Zhao, D. Zhou, J. Rong, L. Zhang, Z. Xia, Myocardial ischemia/reperfusion injury: mechanisms of injury and implications for management (Review), Exp. Ther. Med. 23 (2022) 430, https://doi.org/10.3892/etm.2022.11357.
[19] O. Tantawi, A. Baalbaki, R.E. Asmar, A. Ghauch, A rapid and economical method for the quantification of hydrogen peroxide (H_2O_2) using a modified HPLC apparatus, Sci. Total. Environ. 654 (2019) 107–117, https://doi.org/10.1016/j.scitotenv.2018.10.372.
[20] H. Sheng, E.D. Hermes, X. Yang, D. Ying, A.N. Janes, W. Li, J.R. Schmidt, S. Jin, Electrocatalytic production of H_2O_2 by selective oxygen reduction using earth-abundant cobalt pyrite (CoS_2), ACS. Catal. 9 (2019) 8433–8442, https://doi.org/10.1021/acscatal.9b02546.
[21] R.A. Costa, C.L.M. Morais, T.R. Rosa, P.R. Filgueiras, M.S. Mendonça, I.E.S. Pereira, B.V. Vittorazzi, M.B. Lyra, K.M.G. Lima, W. Romão, Quantification of milk adulterants (starch, H_2O_2, and NaClO) using colorimetric assays coupled to smartphone image analysis, Microchem. J. 156 (2020) 104968, https://doi.org/10.1016/j.microc.2020.104968.
[22] E. Kurowska-Tabor, M. Jaskula, G.D. Sulka, Sensitive amperometric sensing of hydrogen peroxide using Ag nanowire array electrode, Electroanalysis. 27 (2015) 1968–1978, https://doi.org/10.1002/elan.201400741.
[23] M.H. Irani-nezhad, A. Khataee, J. Hassanzadeh, Y. Orooji, A chemiluminescent method for the detection of H_2O_2 and glucose based on intrinsic peroxidase-like activity of WS_2 quantum dots, Molecules. 24 (2019) 689, https://doi.org/10.3390/molecules24040689.
[24] H. Saada, R. Abdallah, J.F. Bergamini, S. Fryars, V. Dorcet, L. Joanny, F. Gouttefangeas, S. Ollivier, G. Loget, Photoelectrochemical sensing of hydrogen peroxide on hematite, ChemElectroChem. 7 (2020) 1155–1159, https://doi.org/10.1002/celc.202000028.

[25] S.G. Liu, S. Liu, S. Yang, Q. Zhao, J. Deng, X. Shi, A facile fluorescent sensing strategy for determination of hydrogen peroxide in foods using a nanohybrid of nanoceria and carbon dots based on the target-promoted electron transfer, Sens. Actuators. B Chem. 356 (2022) 131325, https://doi.org/10.1016/j.snb.2021.131325.

[26] S. Sharma, K. Sharma, A. Kumar, C.S.P. Tripathi, D. Guin, Fabrication of a non-enzymatic electrochemical sensor based on magnesium oxide nanosheets for selective and sensitive detection of hydrogen peroxide in food samples, J. Appl. Electrochem. 54 (2024) 1365–1377, https://doi.org/10.1007/s10800-023-02030-7.

[27] I. Mihailova, M. Krasovska, E. Sledevskis, V. Gerbreders, V. Mizers, A. Ogurcovs, Assessment of oxidative stress by detection of H_2O_2 in rye samples using a CuO- and Co_3O_4-nanostructure-based electrochemical sensor, Chemosensors 11 (2023) 532.

[28] R.S. Alruwais, W.A. Adeosun, Electrochemical detection of hydrogen peroxide using copper-based metal–Organic frameworks: nanoarchitectonics and sensing performance, J. Inorg. Organomet. Polym. 34 (2024) 14–37, https://doi.org/10.1007/s10904-023-02787-6.

[29] L. Naderi, S. Shahrokhian, M.K. Amini, M.H. Kahnamouei, Comparison of electrocatalytic performance of $CuCo_2O_4$ nanorods and nanospheres decorated with Co_3S_4 nanosheets for electrochemical sensing of hydrogen peroxide and glucose in Human serum, ACS. Appl. Nano Mater. 6 (2023), https://doi.org/10.1021/acsanm.2c05164.

[30] N. Khaliq, M.A. Rasheed, M. Khan, M. Maqbool, M. Ahmad, S. Karim, A. Nisar, P. Schmuki, S.O. Cho, G. Ali, Voltage-switchable biosensor with gold nanoparticles on TiO2 nanotubes decorated with CdS quantum dots for the detection of cholesterol and H_2O_2, ACS. Appl. Mater. Interfaces. 13 (2021) 3653–3668, https://doi.org/10.1021/acsami.0c19979.

[31] A. Jasmin, P. Traiwatcharanon, S. Kondee, S.X. Chin, C. Wongchoosuk, An electrochemical sensor based on Fe2O3 quantum dot-decorated Co_3O_4 nanowires for cannabis detection in food, Appl. Phys. A 130 (2024) 763, https://doi.org/10.1007/s00339-024-07927-4.

[32] P. Traiwatcharanon, S. Velmurugan, M. Zacharias, C. Wongchoosuk, Sparked ZnO nanoparticles-based electrochemical sensor for onsite determination of glyphosate residues, J. Nanotechnol. 34 (2023) 415501. https://iopscience.iop.org/article/10.1088/1361-6528/ace3cc/meta.

[33] S. Kondee, W. Pon-On, W. Siriwatcharapiboon, A. Tuantranont, C. Wongchoosuk, CuO/SnS_2 nanoparticles on PEDOT:PSS for nonenzymatic electrochemical glucose sensors, ACS. Appl. Nano Mater. 7 (2024) 6722–6735. https://pubs.acs.org/doi/abs/10.1021/acsanm.4c01093.

[34] P. Traiwatcharanon, W. Pon-On, M. Zacharias, C. Wongchoosuk, Electrochemical copper oxide nanoparticles-based sensor for butachlor plus propanil herbicide detection, Mater. Electron. 35 (2024). https://link.springer.com/article/10.1007/s10854-024-12419-5.

[35] K. Wang, Y. Sun, W. Xu, W. Zhang, F. Zhang, Y. Qi, Y. Zhang, Q. Zhou, B. Dong, C. Li, L. Wang, L. Xu, Non-enzymatic electrochemical detection of H_2O_2 by assembly of CuO nanoparticles and black phosphorus nanosheets for early diagnosis of periodontitis, Sens. Actuators. B Chem. 355 (2022) 131298, https://doi.org/10.1016/j.snb.2021.131298.

[36] Y. Li, H. Chen, R. Huang, D. Deng, X. Yan, L. Luo, An origami microfluidic paper device based on core-shell Cu@Cu2S@N-doped carbon hollow nanocubes, Anal. Chim. Acta 1316 (2024) 342828, https://doi.org/10.1016/j.aca.2024.342828.

[37] J. Song, R. Huang, Y. Chen, D. Deng, X. Yan, L. Luo, Research progress of flexible sweat sensors based on conductive materials, Chinese J. Anal. Chem. 51 (2023) 695–705, https://doi.org/10.19756/j.issn.0253-3820.221623.

[38] Y. Li, K. Huan, D. Deng, L. Tang, J. Wang, L. Luo, Facile synthesis of ZnMn2O4@rGO microspheres for ultrasensitive electrochemical detection of hydrogen peroxide from Human breast cancer cells, ACS. Appl. Mater. Interfaces. 12 (2020) 3430–3437, https://doi.org/10.1021/acsami.9b19126.

[39] V.V. Poliukhova, S. Khan, Z. Qiaohong, J. Zhang, D. Kim, S. Kim, S.H. Cho, ZnS/ZnO nanosheets obtained by thermal treatment of ZnS/ethylenediamine as a Z-scheme photocatalyst for H_2 generation and Cr(VI) reduction, Appl. Surf. Sci. 575 (2022) 151773, https://doi.org/10.1016/j.apsusc.2021.151773.

[40] X. Wen, J. Ni, S. Zeng, Z. Song, W. Qiu, One-pot synthesis of nanoflower-like Zn_2SnS_4 as nanozymes for highly sensitive electrochemical detection of H_2O_2 released by living cells, Chem. Eur. J. 30 (2024), https://doi.org/10.1002/chem.202400700.

[41] R. Boulkroune, M. Sebais, Y. Messai, R. Bourzami, M. Schmutz, C. Blanck, O. Halimi, B. Boudine, Hydrothermal synthesis of strontium-doped ZnS nanoparticles: structural, electronic and photocatalytic investigations, Bull. Mater. Sci. 42 (2019), https://doi.org/10.1007/s12034-019-1905-2.

[42] V. Beena, S.L. Rayar, S. Ajitha, A. Ahmad 3, M.D. Albaqami, F.A.A. Alsabar, M. Sillanpää, Synthesis and characterization of Sr-doped ZnSe nanoparticles for catalytic and biological activities, Water J. 13 (2021) 2189, https://doi.org/10.3390/w13162189.

[43] W. Hu, F. Dong, M. Liu, D. Yang, N. Luo, C. Chen, Photocatalytic reduction of Cr (VI) using a wurtzite/natural sphalerite heterostructure: synergistic effects of exposed active facets, vacancies and a heterophase junction, Appl. Surf. Sci. 550 (2021) 149267, https://doi.org/10.1016/j.apsusc.2021.149267.

[44] R. Boulkroune, M. Sebais, Y. Messai, R. Bourzami, M. Schmutz, C. Blanck, O. Halimi, B. Boudine, Hydrothermal synthesis of strontium-doped ZnS nanoparticles: structural, electronic and photocatalytic investigations, Bull. Mater. Sci. 42 (2019), https://doi.org/10.1007/s12034-019-1905-2.

[45] L. Mao, F. Wang, J. Mao, Polar mesoporous zinc sulfide nanosheets encapsulated in reduced graphene oxide three-dimensional foams for sulfur host, Sci. Rep. 10 (2020), https://doi.org/10.1038/s41598-020-62037-4.

[46] K. Zhang, J. Zhang, X. He, Y. Zhao, A. Zada, A. Peng, K. Qi, Fe_3O_4@MIL-100(Fe) modified ZnS nanoparticles with enhanced sonocatalytic degradation of tetracycline antibiotic in water, Ultrason. Sonochem. 95 (2023) 106409, https://doi.org/10.1016/j.ultsonch.2023.106409.

[47] S.K. Jeong, M.H. Kim, S.Y. Lee, H. Seo, D.K. Choi, Dual active layer a-IGZO TFT via homogeneous conductive layer formation by photochemical H-doping, Nanoscale Res. Lett. 9 (2014), https://doi.org/10.1186/1556-276X-9-619.

[48] J. Dong, X. Zeng, W. Xia, X. Zhang, M. Zhou, C. Wang, Ferromagnetic behavior of non-stoichiometric ZnS microspheres with a nanoplate-netted surface, RSC. Adv. 34 (2017), https://doi.org/10.1039/C7RA02521A.

[49] K.V. Savunthari, S. Shanmugam, Effect of co-doping of bismuth, copper and cerium in zinc ferrite on the photocatalytic degradation of bisphenol A, J. Taiwan. Inst. Chem. Eng. 101 (2019) 105–118, https://doi.org/10.1016/j.jtice.2019.04.042.

[50] V. Poliukhova, S. Khan, Z. Qiaohong, J. Zhang, D. Kim, S. Kim, S.H. Cho, ZnS/ZnO nanosheets obtained by thermal treatment of ZnS/ethylenediamine as a Z-scheme photocatalyst for H_2 generation and Cr(VI) reduction, Appl. Surf. Sci. 575 (2022) 151773, https://doi.org/10.1016/j.apsusc.2021.151773.

[51] P.K. Gopi, B. Muthukutty, S.M. Chen, T.W. Chen, X. Liu, A.A. Alothman, M.A. Alie, S.M. Wabaidur, Platelet-structured strontium titanate perovskite decorated on graphene oxide as a nanocatalyst for electrochemical determination of neurotransmitter dopamine, New. J. Chem. 42 (2020), https://doi.org/10.1039/D0NJ03564E.

[52] G. Carlota, G.C. Lucia, F. Marcos, O. Inmaculada, Non-enzymatic amperometric glucose screen-printed sensors based on copper and copper oxide particles, Appl. Sci. 11 (2021) 10830, https://doi.org/10.3390/app112210830.

[53] G.G. Lee, H.G. Hong, Catalytically synthesized prussian blue by a one-step copolymerization of polydopamine-polypyrrole for electrochemical sensing of hydrogen peroxide, Electrochim. Acta 465 (2023) 142949, https://doi.org/10.1016/j.electacta.2023.142949.

[54] B. Łosiewicz, P. Osak, K. Górka-Kulikowska, J. Maszybrocka, Effect of artificial saliva modification on corrosion resistance of metal oxide coatings on Co-Cr-Mo dental alloy, Mater 17 (2024) 5166, https://doi.org/10.3390/ma17215166.

[55] M.I. González-Sánchez, B. Gómez-Monedero, J. Agrisuelas, J. Iniesta, E. Valero, Highly activated screen-printed carbon electrodes by electrochemical treatment with hydrogen peroxide, Electrochem. Commun. 91 (2018) 36–40, https://doi.org/10.1016/j.elecom.2018.05.002.

[56] A.L. Sanford, S.W. Morton, K.L. Whitehouse, H.M. Oara, L.Z. Lugo-Morales, J. G. Roberts, L.A. Sombers, Voltammetric detection of hydrogen peroxide at carbon Fiber microelectrodes, Anal. Chem. 82 (2010) 5205–5210, https://doi.org/10.1021/ac100536s.

[57] A. Laroussi, N. Raouafi, V.M. Mirsky, Electrocatalytic sensor for hydrogen peroxide based on immobilized benzoquinone, Electroanalysis. 33 (2021) 2062–2070, https://doi.org/10.1002/elan.202100113.

[58] A. Mahieddine, L. Adnane-Amara, A novel non-enzymatic electrochemical sensor based on NiS/Co_3S_4@h-Ni NWs core-shell electrode for glucose detection in human serum, Mater. Chem. Phys. 302 (2023) 127730, https://doi.org/10.1016/j.matchemphys.2023.127730.

[59] A. Laroussi, N. Raouafi, V.M. Mirsky, Electrocatalytic sensor for hydrogen peroxide based on immobilized benzoquinone, Electroanalysis. 33 (2021) 2062–2070, https://doi.org/10.1002/elan.202100113.

[60] M.R. Mahmoudian, Y. Alias, W.J. Basirun, M. Ebadi, Preparation of ultra-thin polypyrrole nanosheets decorated with Ag nanoparticles and their application in hydrogen peroxide detection, Electrochim. Acta 72 (2012) 46–52, https://doi.org/10.1016/j.electacta.2012.03.144.

[61] L. Lorencova, T. Bertok, E. Dosekova, A. Holazova, D. Paprckova, A. Vikartovska, V. Sasinkova, J. Filip, P. Kasak, M. Jerigiva, D. Velic, K.A. Mahmoud, J. Tkac, Electrochemical performance of Ti3C2Tx MXene in aqueous media: towards ultrasensitive H_2O_2 sensing, Electrochim. Acta 235 (2017) 471–479, https://doi.org/10.1016/j.electacta.2017.03.073.

[62] S. Majumder, B. Saha, S. Dey, R. Mondal, S. Kumar, S. Banerjee, A highly sensitive non-enzymatic hydrogen peroxide and hydrazine electrochemical sensor based on 3D micro-snowflake architectures of α-Fe_2O_3, RSC. Adv. 65 (2016), https://doi.org/10.1039/C6RA10470C.

[63] D. Li, L. Meng, S. Dang, D. Jiang, W. Shi, Hydrogen peroxide sensing using Cu_2O nanocubes decorated by Ag-Au alloy nanoparticles, J. Alloys. Compd. 690 (2017) 1–7, https://doi.org/10.1016/j.jallcom.2016.08.108.

[64] M.R. Mahmoudian, Y. Alias, W.J. Basirun, M. Ebadi, Preparation of ultra-thin polypyrrole nanosheets decorated with Ag nanoparticles and their application in hydrogen peroxide detection, Electrochim. Acta 72 (2012) 46–52, https://doi.org/10.1016/j.electacta.2012.03.144.

[65] A.K. Diallo, L. Djeghlaf, L. Mazenq, J. Launay, W. Sant, P. Temple-Boyer, Development of pH-based ElecFET biosensors for lactate ion detection, Biosens. Bioelectron. 40 (2013) 291–296, https://doi.org/10.1016/j.bios.2012.07.063.

[66] T. Dam, V. Anh, W. Olthuis, P. Bergveld, Electroactive gate materials for a hydrogen peroxide sensitive ^{E}MOSFET, IEEe Sens. J. 2 (2002) 26–33, https://doi.org/10.1109/7361.987058.

[67] X. Jiang, Y. Wu, X. Mao, X. Cui, L. Zhu, Amperometric glucose biosensor based on integration of glucose oxidase with platinum nanoparticles/ordered mesoporous carbon nanocomposite, Sens. Actuators. B Chem. 153 (2011) 158–163, https://doi.org/10.1016/j.snb.2010.10.023.

[68] D. Xiang, L. Yin, J. Ma, E. Guo, Q. Li, Z. Li, K. Liu, Amperometric hydrogen peroxide and glucose biosensor based on $NiFe_2$/ordered mesoporous carbon nanocomposites, Analyst 2 (2015), https://doi.org/10.1039/C4AN01549E.

[69] A.A. Dutta, S.K. Maji, D.N. Srivastava, A. Mondal, P. Biswas, P. Pual, B. Adhikary, Peroxidase-like activity and amperometric sensing of hydrogen peroxide by Fe_2O_3

and Prussian Blue-modified Fe_2O_3 nanoparticles, J. Mol. Catal. A Chem. 360 (2012) 71–77, https://doi.org/10.1016/j.molcata.2012.04.011.
[70] E. Song, J.W. Choi, A selective hydrogen peroxide sensor based on chemiresistive polyaniline nanowires modified with silver catalytic nanoparticles, J. Micromech. Microeng. 24 (2014), https://doi.org/10.1088/0960-1317/24/6/065004.
[71] E. Song, R.P. Tortorich, T.H. Costa, J.W. Choi, Inkjet printing of conductive polymer nanowire network on flexible substrates and its application in chemical sensing, Microelectron. Eng. 145 (2015) 143–148, https://doi.org/10.1016/j.mee.2015.04.004.
[72] M. Shafa, I. Ahmad, S. Hussain, M. Asif, Y. Pan, R. Zairov, A.A. Alothman, M. Ouladsmane, Z. Ullah, N. Ullah, C. Lai, U. Jabeen, Ag-Cu nanoalloys: an electrochemical sensor for H_2O_2 detection, Surf. Interfaces. 36 (2023) 102616, https://doi.org/10.1016/j.surfin.2022.102616.
[73] M. Merisalu, J. Kruusma, C.E. Banks, Metallic impurity free carbon nanotube paste electrodes, Electrochem. Commun. 12 (2010) 144–147, https://doi.org/10.1016/j.elecom.2009.11.009.